MODELING, IDENTIFICATION AND CONTROL, 2002, VOL. 23, NO. 4, 275–298
doi:10.4173/mic.2002.4.3

Tutorial on Feedback Control of Flows, Part II: Diagnostics and Feedback Control of Mixing*

OLE MORTEN AAMO and THOR I. FOSSEN†

Keywords: *Flow control, feedback, mixing*

Control of fluid flows span a wide variety of specialities. In Part II of this tutorial, we focus on diagnostics of mixing and the problem of enhancing mixing by boundary feedback control. Diagnostic tools from dynamical systems theory are presented that enable detection and quantification of chaotic transport in periodically perturbed systems. However, real systems are generally not periodic, and available measurements or simulations are finite in time. A method for quantifying mixing in finite-time velocity fields is discussed, and applied to data obtained from simulations of the 2D controlled channel flow. Mixing has traditionally been brought on by open-loop control strategies, such as stirring, jet injection or mixing valves. Applications of active feedback to mixing problems are scarce in the literature, but the idea is currently drawing attention from various research groups. Feedback laws for the purpose of mixing enhancement in 2D and 3D pipe flow are presented, and simulations show that they induce strong mixing.

1. Introduction

In many engineering applications, the mixing of two or more fluids is essential to obtaining good performance in some downstream process (a prime example is the mixing of air and fuel in combustion engines (Ghoniem and Ng, 1987, Annaswamy and Ghoniem, 1995). As a consequence, mixing has been the focus of much research, but without reaching a unified theory, either for the generation of flows that mix well due to external forcing, or for the quantification of mixing in such flows, see Ottino (1989) for a review. Approaches range from experimental design and testing to modern applications of dynamical systems theory. The latter was initiated by Aref (1984), who studied chaotic advection in the setting of an incompressible, inviscid fluid contained in a (2D) circular domain, and agitated by a point vortex. This flow is commonly called the blinking vortex flow. Ottino and coworkers studied a number of various flows, examining mixing properties based on dynamical systems techniques (Chien *et al.*, 1986, Khakhar *et al.*, 1986, Leong and Ottino, 1989, Swanson and Ottino, 1990). Later Rom-Kedar *et al.* (1990) applied Melnikov's method and KAM (Kolmogorov-Arnold-Moser) theory to quantify transport in a flow governed by an oscillating vortex pair. For a general treatment of dynamical systems theory, see, for instance, Guckenheimer and Holmes (1983), Wiggins (1990), and for background material related to transport in dynamical systems, see Wiggins (1992). An obvious shortcoming of this theory is the requirement that the flow must be periodic, as such methods rely on the existence of a Poincaré map for which some periodic orbit of the flow induces a hyperbolic fixed point. Another shortcoming is that they can only

*Submitted to MIC on 10 January, 2002.
†Department of Engineering Cybernetics, Norwegian University of Science and Technology, N-7491 Trondheim, Norway.

handle small perturbations from integrability, whereas effective mixing usually occurs for large perturbations (Ottino, 1990). A third shortcoming is that traditional dynamical systems theory is concerned with asymptotic, or long-time, behavior, rather than quantifying rate processes which are of interest in mixing applications. In order to overcome some of these shortcomings, recent advances in dynamical systems theory have focused on finding coherent structures and invariant manifolds in experimental datasets, which are finite in time and generally aperiodic. This has led to the notions of finite-time hyperbolic trajectories with corresponding finite-time stable and unstable manifolds (Haller and Poje, 1998, Haller, 2000, Haller and Yuan, 2000, Haller, 2001). The results include estimates for the transport of initial conditions across the boundaries of coherent structures. In Poje and Haller (1999) these concepts were applied to a time-dependent velocity field generated by a double-gyre ocean model, in order to study the fluid transport between dynamic eddies and a jet stream. An application to meandering jets was described in Miller *et al.* (1997). Another method for identifying regions in a flow that have similar finite-time statistical properties based on ergodic theory was developed and applied in Mezić (1994), Malhotra *et al.* (1998), Mezić and Wiggins (1999). The relationship between the two methods mentioned, focusing on geometrical and statistical properties of particle motion, respectively, was examined in Poje *et al.* (1999).

As these developments have partly been motivated by applications in geophysical flows, they are diagnostic in nature and lend little help to the problem of *generating* a fluid flow that mixes well. The problem of generating effective mixing in a fluid flow is usually approached by trial and error using various 'brute force' open-loop controls, such as mechanical stirring, jet injection or mixing valves. However, in the recent papers (D'Allessandro *et al.*, 1998, D'Allessandro *et al.*, 1999), control systems theory was used to rigorously derive the mixing protocol that maximizes entropy among all the possible periodic sequences composed of two shear flows orthogonal to each other. In Noack *et al.* (2000), the optimal vortex trajectory in the flow induced by a single vortex in a corner subject to a controlled external strain field is found using tools from dynamical systems theory. The resulting trajectory is stabilized using control theory.

In Aamo *et al.* (2001), active feedback control was applied in order to enhance existing instability mechanisms in a 2D model of plane channel flow. By applying boundary control intelligently in a feedback loop, mixing was considerably enhanced with relatively small control effort. The control law was decentralized and designed using Lyapunov stability analysis. These efforts have recently been extended successfully to 3D pipe flow (Balogh *et al.*, 2001), where it is also shown that the control law has certain optimality properties.

In a recent paper by Bamieh *et al.* (2001), the authors present a framework for destabilization, in an optimal manner, of linear time-invariant systems for the purpose of achieving mixing enhancement.

The remainder of this paper presents selected works in detail, with particular emphasis on those using active feedback control for mixing enhancement.

2. What is Mixing?

A number of inherently different processes constitute what is called mixing. Ottino (1989) distinguishes between three sub-problems of mixing: (i) mixing of a single fluid (or similiar fluids) governed by the stretching and folding of material elements;

(ii) mixing governed by diffusion or chemical reactions; and (iii) mixing of different fluids governed by the breakup and coalescence of material elements. Of course, all processes may be present simultaneously. In the first sub-problem, the interfaces between the fluids are passive (Aref and Tryggvason, 1984), and the mixing may be determined by studying the movement of a passive tracer, or dye, in a homogeneous fluid flow. This is the problem we are interested in here.

3. Diagnostics of Mixing

3.1. *Chaotic advection in the blinking vortex flow*

The application of dynamical systems theory to problems in mixing was initiated by Aref (1984), who studied advection of passive tracer particles in the setting of an incompressible, inviscid fluid, contained in a 2D circular domain. It was shown in that reference, that a simple-looking, deterministic Eulerian velocity field may produce an essentially stochastic response in the Lagrangian advection characteristics of a passive tracer. This behavior is referred to as *chaotic advection*. The flow is driven by a point vortex, whose motion in a circular domain of radius a, is denoted $z(t)$, and it's strength is denoted Γ. The function $z(t)$ is referred to as the *stirring protocol*. A point in the domain is denoted ζ, so that $\zeta = x + iy$. The flow is represented by a complex valued function $f(\zeta)$, such that

$$w = f(\zeta) = \phi + i\psi$$

where ϕ is the potential function and ψ is the stream function. A point vortex at the origin with strength Γ is given by

$$w = \frac{\Gamma}{2\pi i} \ln \zeta$$

If the point vortex is allowed to move according to $z(t)$, we get

$$w = \frac{\Gamma}{2\pi i} \ln (\zeta - z)$$

For a circular domain with radius a, we superpose the image of the point vortex at $z(t)$ to obtain

$$w = \frac{\Gamma}{2\pi i} \ln (\zeta - z) + \left(-\frac{\Gamma}{2\pi i} \ln \left(\zeta - \frac{a^2}{\bar{z}} \right) \right) = \frac{\Gamma}{2\pi i} \ln \left(\frac{\zeta - z}{\zeta - \frac{a^2}{\bar{z}}} \right)$$

Consider a particle p, placed into the domain. We denote it's position by

$$\zeta_p = x + iy$$

The velocity of the particle is given by

$$\dot{\bar{\zeta}}_p = u - iv = \frac{\partial \phi}{\partial x} + i \frac{\partial \psi}{\partial x} = \frac{\partial w}{\partial x} = \frac{\Gamma}{2\pi i} \left(\frac{1}{\zeta_p - z} - \frac{1}{\zeta_p - \frac{a^2}{\bar{z}}} \right) \tag{1}$$

By solving equation (1) for an array of particles, we can now visualize the mixing properties of the flow for various stirring protocols. In Aref (1984), the particular case when

$$z(t) = \begin{cases} b & \text{for } nT \leqslant t(n+\frac{1}{2})T \\ -b & \text{for } (n+\frac{1}{2})T \leqslant t(n+1)T \end{cases}, \quad n = 0, 1, 2, 3, \ldots \tag{2}$$

is studied in detail. b is a constant (possibly complex) contained in the domain, and T is a positive real constant specifying the period of $z(t)$. The flow resulting from the stirring protocol equation (2) is called the blinking vortex flow. The evolution governed by equation (1) induces a mapping of the disk $|\zeta| \leqslant a$ onto itself, defined by $M: \zeta(t) \to \zeta(t+T)$. The mapping M is referred to as a Poincaré map. Denoting an initial set of points as P_0, and applying the map iteratively to obtain the sets

$$P_n = M(P_{n-1}), n = 1, 2, 3, \ldots$$

we define the set of visited points after N iterations as

$$\mathscr{P}_N = \bigcup_{0 \leqslant n \leqslant N} P_n$$

Figure 1 shows $\mathscr{P}_{2000}$ for $b = 0.5$, $P_0 = [-0.35, -0.2, -0.05, 0.1i, 0.2i, \ldots, 0.8i, 0.9i, 0.05, 0.2, 0.35]$, and for 9 different periods ($T \in [0.05, 0.1, 0.125, 0.15, 0.20, 0.35, 0.5, 1, 1.5]$). For $T = 0.05$, $\mathscr{P}_{2000}$ appears very regular, and the points visit a very small area of the total domain. This suggests that a blob of tracer material put into this flow, would be contained in a limited area given by the lines in the figure. As T is increased, regions of chaotic behavior appear, and the size of these regions increase with increasing T. When $T = 1.5$, no trace of regularity can be seen. Next, we consider the kind of stirring experiment which would be carried out in a real device. This is done by introducing a blob of tracer material into the fluid at $t = 0$, and watch it evolve with time. Figure 2 shows the initial configuration of particles representing a square blob for the study of the mixing properties of equation (2). 10 000 particles are evenly distributed in the box $[-0.125, 0.125] \times [0, 0.25]$. The position of the point vortex is again chosen as $b = 0.5$. Figure 3 shows the configuration of particles for 4 different time instances ($t \in [3, 6, 9, 12]$) for 3 different periods ($T \in [0.1, 1, 3]$). As anticipated in Figure 1, the blob is contained in a very limited area for $T = 0.1$, and the shape of the area is easily recognized to be formed by the lines appearing in Figure 1. Thus, it is shown how the study of a dynamical system can be reduced to the study of a map, for which redundant dynamics are filtered out so that emphasis is put on the underlying structures that govern mixing and transport.

3.2. *Particle transport in the mixing region of the oscillating vortex pair flow*

3.2.1. *The oscillating vortex pair flow* In Rom-Kedar (1990) dynamical systems theory is applied in a mathematically rigorous manner in order to study the mixing properties in a 2D model flow governed by a vortex pair in the presence of an oscillating external strain-rate field. The vortices have strength $\pm\Gamma$, and are initially separated by a distance $2d$ in the y direction. The stream function for the flow in a frame moving with the average velocity of the vortices is

$$\Psi = -\frac{\Gamma}{4\pi} \log \left\{ \frac{(x-x_v)^2 + (y-y_v)^2}{(x-x_v)^2 + (y+y_v)^2} \right\} - V_v y + \varepsilon xy \sin(\omega t)$$

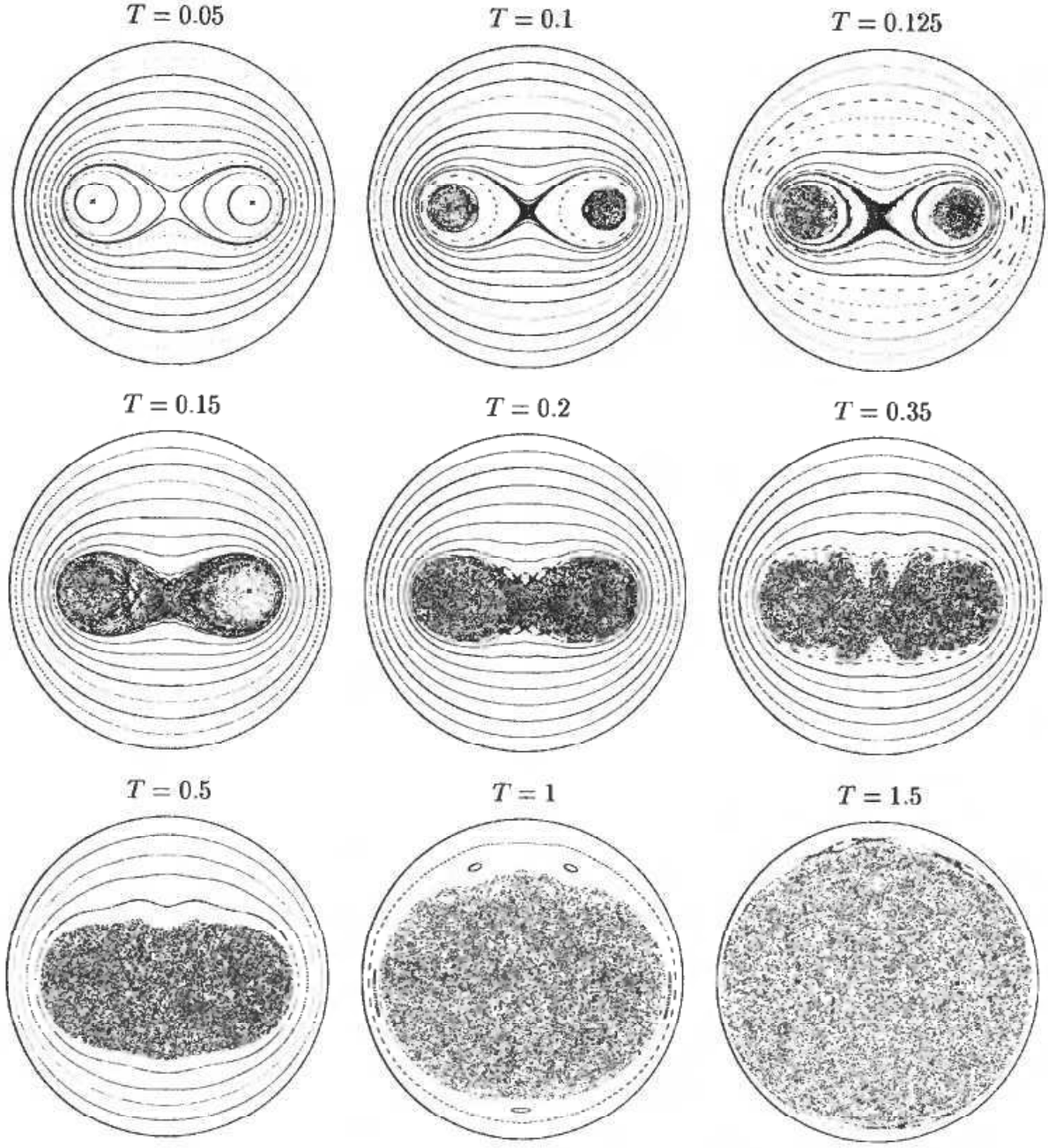

Figure 1. Iterated-map results ($\mathscr{P}_{2000}$) for $T \in [0.05, 0.1, 0.125, 0.15, 0.2, 0.35, 0.5, 1, 1.5]$.

where $(x_v(t), y_v(t))$ and $(x_v(t), -y_v(t))$ are the vortex positions, ε is the strain rate and V_v is the average velocity of the vortex pair. For $\varepsilon = 0$, $x_v(t) = 0$, $y_v(t) = d$ and $V_v = \Gamma/4\pi d$. Introducing appropriate scaling of the variables, and defining $\gamma = \Gamma/2\pi\omega d^2$ and $v_v = 2\pi d V_v/\Gamma$, we obtain the dimensionless equations for particle motion

$$\frac{dx}{dt} = -\left(\frac{y - y_v}{(x - x_v)^2 + (y - y_v)^2} - \frac{y + y_v}{(x - x_v)^2 + (y + y_v)^2}\right) - v_v + \frac{\varepsilon x}{\gamma}\sin(t/\gamma) \qquad (3)$$

$$\frac{dy}{dt} = (x - x_v)\left(\frac{1}{(x - x_v)^2 + (y - y_v)^2} - \frac{1}{(x - x_v)^2 + (y + y_v)^2}\right) - \frac{\varepsilon y}{\gamma}\sin(t/\gamma) \qquad (4)$$

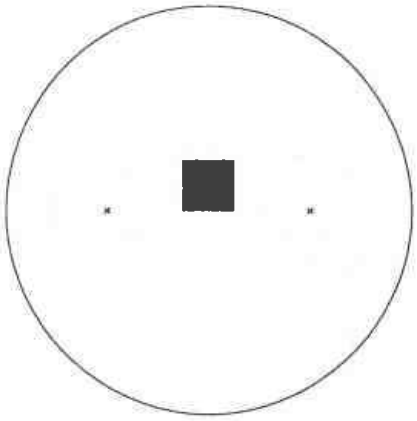

Figure 2. Initial configuration of particles for studying the mixing properties of the blinking vortex flow. The position of the point vortex is indicated by the two crosses (×).

The vortex positions are governed by

$$\frac{dx_v}{dt} = \frac{1}{2y_v} - v_v + \frac{\varepsilon x_v}{\gamma}\sin(t/\gamma)$$

$$\frac{dy_v}{dt} = -\frac{\varepsilon y_v}{\gamma}\sin(t/\gamma)$$

This flow approximates the motion in the vicinity of a vortex pair moving in a wavy-walled channel. In the perturbation analysis that follows, ε is assumed to be small. The right hand side of equations (3)–(4) can be expanded in powers of ε to obtain

$$\dot{x} = f_1(x,y) + \varepsilon g_1(x,y,t/\gamma;\gamma) + O(\varepsilon^2) \tag{5}$$

$$\dot{y} = f_2(x,y) + \varepsilon g_2(x,y,t/\gamma;\gamma) + O(\varepsilon^2) \tag{6}$$

where

$$f_1(x,y) = -\frac{y-1}{I_-} + \frac{y+1}{I_+} - \frac{1}{2}$$

$$f_2(x,y) = x\left(\frac{1}{I_-} - \frac{1}{I_+}\right)$$

$$g_1(x,y,t/\gamma;\gamma) = (\cos(t/\gamma)-1)\left(\frac{1}{I_-} + \frac{1}{I_+} - \frac{2(y+1)^2}{I_+^2}\right)$$

$$+\frac{x}{\gamma}\sin(t/\gamma)\left(\gamma^2\left(\frac{y-1}{I_-^2} - \frac{y+1}{I_+^2}\right) + 1\right) - \frac{1}{2}$$

$$g_2(x,y,t/\gamma;\gamma) = 2x(\cos(t/\gamma)-1)\left(\frac{y-1}{I_-^2} + \frac{y+1}{I_+^2}\right)$$

$$+\frac{1}{\gamma}\sin(t/\gamma)\left(\frac{\gamma^2}{2}\left(\frac{1}{I_-^2} - \frac{1}{I_+}\right) - x^2y^2\left(\frac{1}{I_-^2} - \frac{1}{I_+^2}\right) - y\right)$$

$$I_+ = x^2 + (y+1)^2,\ I_- = x^2 + (y-1)^2$$

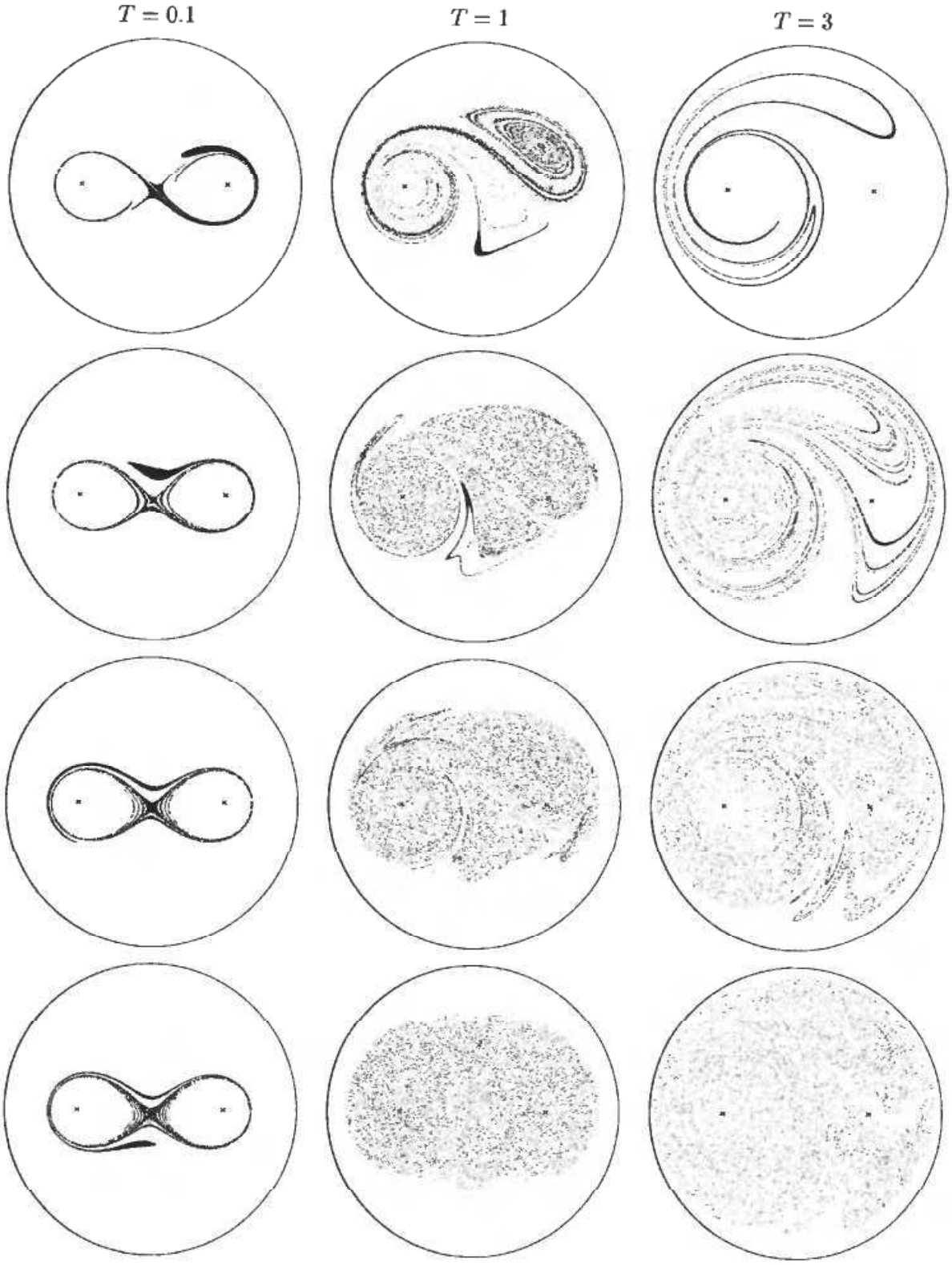

Figure 3. Configuration of particles in the blinking vortex flow for 4 different time instances ($t \in [3, 6, 9, 12]$) for 3 different periods ($T \in [0.1, 1, 3]$).

The streamlines of the unperturbed flow ($\varepsilon = 0$) are shown in Figure 4. For this case, there are two hyperbolic fixed points, p_- and p_+, connected by the limiting streamlines defined by

$$\Psi_l : \Psi(x,y)|_{\varepsilon=0} = 0,\ |x| < \sqrt{3},\ y < 0$$

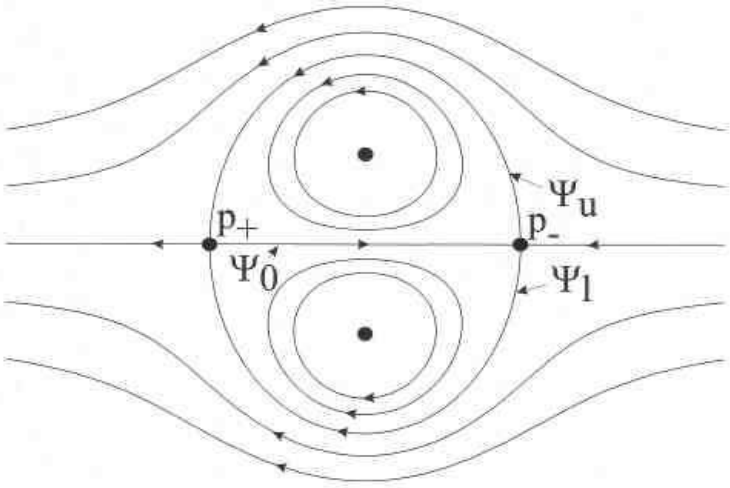

Figure 4. Streamline of the unperturbed vortex pair flow.

$$\Psi_0 : \Psi(x,y)|_{\varepsilon=0} = 0,\ |x| < \sqrt{3},\ y = 0$$

$$\Psi_u : \Psi(x,y)|_{\varepsilon=0} = 0,\ |x| < \sqrt{3},\ y > 0.$$

The particle motions on the interior of the limiting streamlines $\Psi_l \cup \Psi_u \cup p_- \cup p_+$ are qualitatively different from those on the exterior. Also, since streamlines cannot cross (for $\varepsilon = 0$), there is no transport between the interior and the exterior of the limiting streamlines. We are interested in analysing how this picture changes when the strain rate field is applied ($\varepsilon \neq 0$).

3.2.2. *The Poincaré map* We may rewrite the time-varying system equations (5)–(6) as an equivalent time-invariant system by introducing the state $\theta = t/\gamma \bmod 2\pi$. Thus, the system equations (5)–(6) can be written as

$$\dot{x} = f_1(x,y) + \varepsilon g_1(x,y,\theta;\gamma) + O(\varepsilon^2) \tag{7}$$

$$\dot{y} = f_2(x,y) + \varepsilon g_2(x,y,\theta;\gamma) + O(\varepsilon^2) \tag{8}$$

$$\dot{\theta} = 1/\gamma \tag{9}$$

which is now a three-dimensional time-invariant system. A two-dimensional global cross section of the three-dimensional state space of equations (7)–(9) can be defined by

$$\Sigma_{\tilde{\theta}} = \{(x,y,\theta) | \theta = \tilde{\theta} \in [0, 2\pi)\}$$

on which we define the Poincaré map

$$\begin{gathered} T_{\tilde{\theta}} : \Sigma_{\tilde{\theta}} \to \Sigma_{\tilde{\theta}} \\ (x(\tilde{\theta}), y(\tilde{\theta})) \mapsto (x(\tilde{\theta} + 2\pi), y(\tilde{\theta} + 2\pi)) \end{gathered} \tag{10}$$

In the unperturbed case, the orbits of the Poincaré map are sequences of discrete points lying on the streamlines shown in Figure 4. Thus, the streamlines are invariant manifolds of the map. Orbits starting on Ψ_l, Ψ_0 and Ψ_u are heteroclinic orbits, and the points p_- and p_+ are fixed points of the map. Orbits on Ψ_l and Ψ_u approach p_+

in positive time, and $\Psi_l \cup \Psi_u \cup p_+$ is therefore the stable manifold of p_+, denoted W^s_+. Similarly, $\Psi_l \cup \Psi_u \cup p_-$ is the unstable manifold of p_-, denoted W^u_-. The unstable manifold of p_+, denoted W^u_+, is $\{(x,y)|x<\sqrt{3}, y=0\}$, and the stable manifold of p_-, denoted W^s_-, is $\{(x,y)|x>-\sqrt{3}, y=0\}$. Clearly, W^s_+ and W^u_- intersect along Ψ_l and Ψ_u, creating a barrier to transport between the interior and exterior of the limiting streamlines. For sufficiently small ε, p_+ and p_- persist as fixed points of the Poincaré map equation (10), denoted $p_{+,\varepsilon}$ and $p_{-,\varepsilon}$, respectively. Their stable and unstable manifolds, W^s_+, W^s_-, W^u_+ and W^u_- also persist to become the stable and unstable manifolds of $p_{+,\varepsilon}$ and $p_{-,\varepsilon}$. They are denoted $W^s_{+,\varepsilon}$, $W^s_{-,\varepsilon}$, $W^u_{+,\varepsilon}$ and $W^u_{-,\varepsilon}$, respectively. Due to symmetry about the x-axis, $y=0$ is an invariant manifold for all ε, which implies that the stable manifold of $p_{-,\varepsilon}$ and the unstable manifold of $p_{+,\varepsilon}$ always coincide on the line connecting the two fixed points. $W^s_{+,\varepsilon}$ and $W^u_{-,\varepsilon}$, on the other hand, may not coincide in the perturbed case. It is possible for $W^s_{+,\varepsilon}$ and $W^u_{-,\varepsilon}$ to intersect at an isolated point, which implies, by invariance of $W^s_{+,\varepsilon}$ and $W^u_{-,\varepsilon}$, that they must also intersect at every iterate of the Poincaré map and it's inverse. Thus, $W^s_{+,\varepsilon}$ and $W^u_{-,\varepsilon}$ may intersect at infinitely many discrete points, leading to a geometry like the one shown in Figure 5. If this is the case, the barrier that is present in the unperturbed case splits open, and transport of fluid accross it becomes possible. This behavior of the stable and unstable manifolds is also reminiscent of chaotic particle motion.

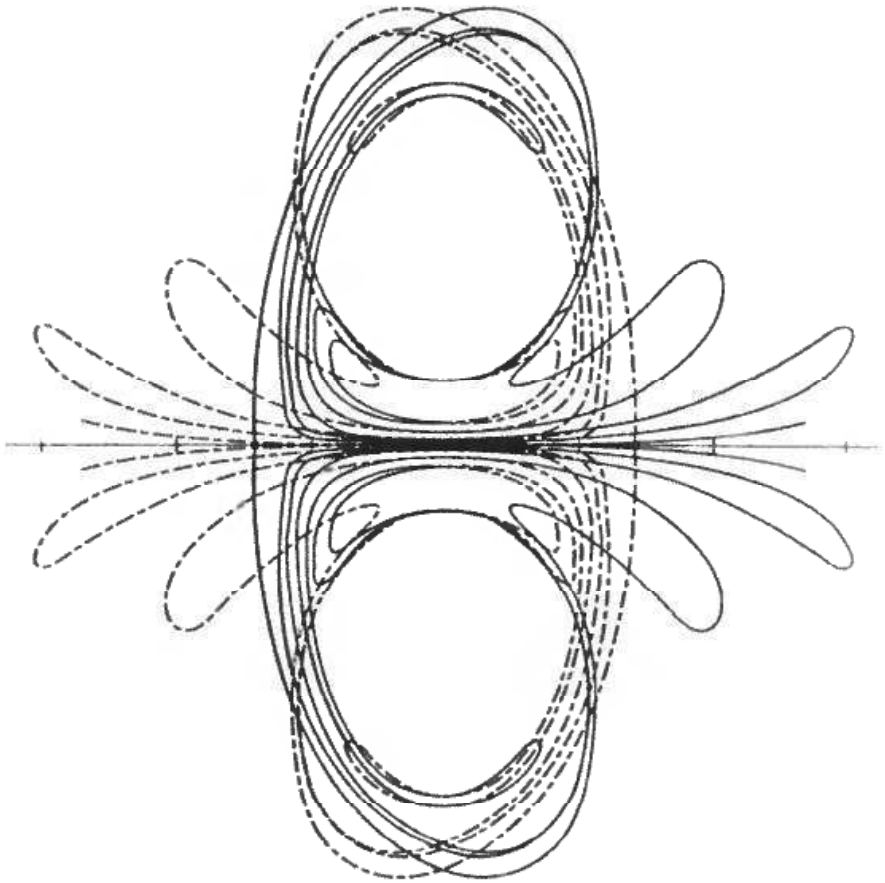

Figure 5. A Poincaré section of the oscillating vortex pair flow, showing the unstable (solid line) and stable (dashed line) manifolds of the two hyperbolic fixed points. Due to the tangling of the manifolds, this image is also referred to as the *homoclinic tangle.*

3.2.3. *Melnikov's method* The existence of an isolated point of intersection of $W^s_{+,\varepsilon}$ and $W^u_{-,\varepsilon}$ can be established by Melnikov's method (Wiggins, 1990), which relates the signed distance between the two manifolds to the so-called Melnikov function according to

$$d(t_0,\varepsilon) = \varepsilon \frac{M(t_0)}{\|f(q_u(-t_0))\|} + O(\varepsilon^2)$$

where $q_u(t)$ is the heteroclinic particle trajectory of the unperturbed velocity field, coinciding with Ψ_u of Figure 4, t_0 parametrizes distance along Ψ_u, and

$$\|f(q_u(-t_0))\| = \sqrt{f_1(q_u(-t_0))^2 + f_2(q_u(-t_0))^2}$$

$M(t_0)$ is the Melnikov function defined as

$$M(t_0) = \int_{-\infty}^{\infty} \{f_1(q_u(t))g_2(q_u(t), t+t_0) - f_2(q_u(t))g_1(q_u(t), t+t_0)\}dt$$

The result of Melnikov states that simple zeros of $M(t_0)$ imply simple zeros of $d(t_0,\varepsilon)$ (for sufficiently small ε). In Rom-Kedar *et al.* (1990), the Melnikov function for the system at hand is computed numerically to obtain

$$M(t_0) = \frac{F(\gamma)}{\gamma}\sin(t_0/\gamma)$$

with $F(\gamma)$ plotted in Figure 6. For any fixed $\gamma \neq \gamma^*$, $M(t_0)$ has an infinite number of simple zeros, corresponding to transverse intersections of $W^s_{+,\varepsilon}$ and $W^u_{-,\varepsilon}$. This confirms the geometry shown in Figure 5. Studying the dynamics associated with the tangling of the stable and unstable manifolds of $p_{+,\varepsilon}$ and $p_{-,\varepsilon}$, can further quantify

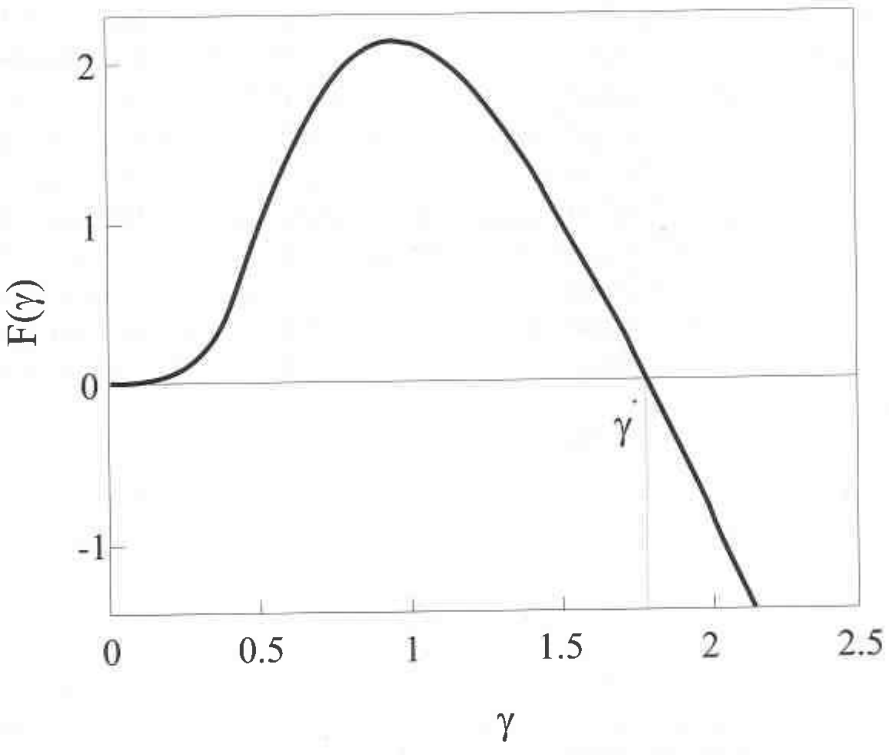

Figure 6. Graph of $F(\gamma)$ appearing in the Melnikov function.

the particle transport taking place. This involves the motion of so-called *lobes*, and the area of these lobes quantifies transport. Again, for sufficiently small ε, the Melnikov function is a measure of the area of the lobes. We will not persue this here, but refer the reader to Rom-Kedar (1990) for further details.

3.3. *Diagnostic tools for finite-time mixing*

In time-periodic advection models, it is enough to know the velocity for finite times (e.g. for one period) to reproduce its infinite-time history. As a result, transport can be studied through the lobe dynamics of stable and unstable manifolds of appropriate Poincaré maps, as was demonstrated in the previous sections. However, for real flows, which in general are not periodic, one would have to know the velocity field for infinite times in order to define stable and unstable manifolds. This fact rules out the study of experimental datasets, both those consisting of measurements of actual flows, as well as those produced in a computer simulation. In a series of papers Haller and Poje (1998), Poje *et al.* (1999), Poje and Haller (1999), Haller (2000), Haller and Yuan (2000), Haller (2001), Haller and coworkers introduced and applied the notions of finite-time stable and unstable manifolds. The essentials of this new theory are outlined below.

3.3.1. *Coherent structures* A real flow will contain regions having different dynamical behavior. These regions are referred to as *Lagrangian coherent structures*. In Section 3.2 we encountered two fundamentally different dynamical behaviors in the oscillating vortex pair flow. One was the rotational motion occuring in the interior of the separating streamlines Ψ_l and Ψ_u, and the other was the translational motion occuring in the exterior of the separating streamlines. Thus, the regions in the interior and exterior of the separating streamlines are examples of coherent structures. The stable and unstable manifolds of the two fixed points coincided on the separating streamlines in the unperturbed case. In the perturbed case, however, they did not coincide, but intersected transversally at an infinite number of discrete points, leading to the formation of lobes whose dynamics is the mechanism by which transport between the interior and the exterior of the boundaries occurs. Such boundaries between coherent structures in the flow appear to be the locations in the flow where material blobs are stretched and folded most extensively. Extensive stretching and folding are reminiscent of effective mixing. Blobs of particles that travel together in the vicinity of coherent structure boundaries will in certain cases suddenly depart in opposite directions leading to local stretching *across* the boundary, as illustrated in Figure 7. In other cases the blob will become thinner and thinner as it is stretched *along* the

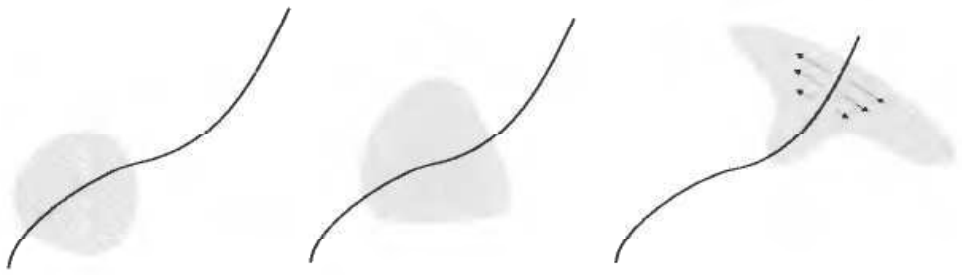

Figure 7. Stretching across a coherent structure boundary.

Figure 8. Stretching along a coherent structure boundary leading to folding.

coherent structure boundary leading, eventually, to folding due to the global geometry of the boundary, as illustrated in Figure 8. For these reasons, it is of interest to be able to localize the boundaries of coherent structures in a given finite-time dataset.

3.3.2. *Material lines and surfaces* Consider the two-dimensional velocity field, $u(x,t)$, with the corresponding particle motion

$$\dot{x} = u(x, t) \tag{11}$$

on some *finite-time* interval $[t_{-1}, t_1]$. Given a curve of initial conditions, Γ_{t_0}, on the state space, later images of Γ_{t_0} under the motion (11), denoted Γ_t, are called *material lines*. Augmenting the state space with the time variable, the evolving curve, Γ_t, spans a two-dimensional surface in the extended state space (x, t). This surface is called a *material surface*, and denoted M (see Figure 9 for a graphical sketch). In order to study the stability of M, we need to linearize the extended flow map, $\mathscr{F}^\tau$, along M. The extended flow map is given by

$$\mathscr{F}^\tau : \begin{pmatrix} x_0 \\ t_0 \end{pmatrix} \mapsto \begin{pmatrix} x(t_0 + \tau; t_0, x_0) \\ t_0 + \tau \end{pmatrix}$$

We denote the linearized extended flow map by $D\mathscr{F}^\tau$.

3.3.3. *Stability properties of material surfaces* M is called an unstable material surface on the time interval I_u if there is a positive exponent λ_u such that for any sufficiently

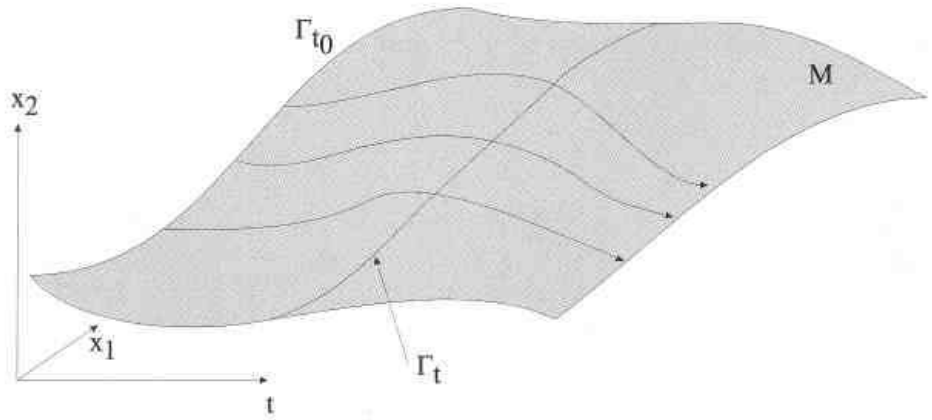

Figure 9. A material surface M spanned out by the material line Γ_t.

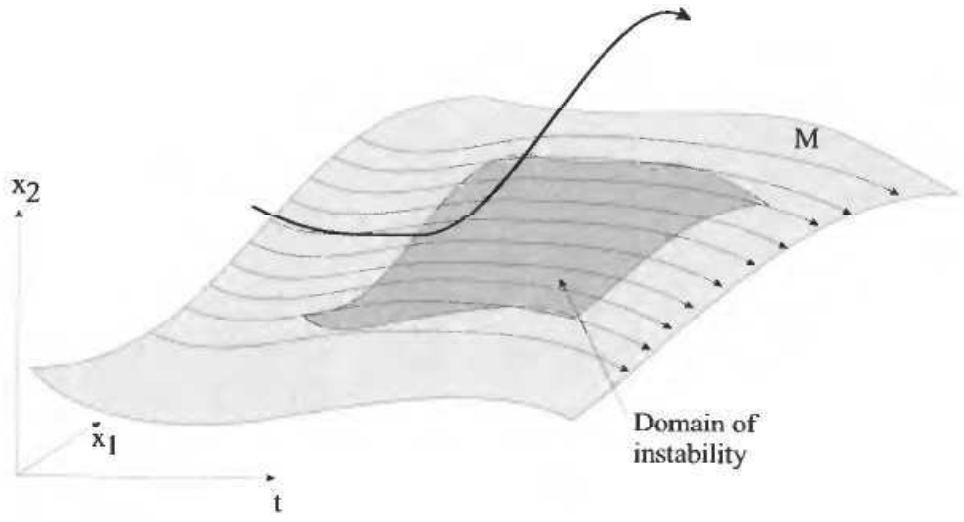

Figure 10. An unstable material surface repelling nearby trajectories.

close initial condition $p(\tau) = (x(\tau), \tau)$ and for any small time step $h > 0$, with $\tau \in I_u$ and $\tau + h \in I_u$, we have

$$\text{dist}(p(\tau + h), M) \geqslant \text{dist}(p(\tau), M) e^{\lambda_u h}$$

So, if $\mathcal{N}(p, t)$ is a unit normal to M at the point (p, t) in the extended state space, then M is an unstable material surface over I_u if for all $\tau, \tau + h \in I_u$ and for all initial conditions $(x_0, \tau) \in M$, we have

$$|\mathcal{N}(x(\tau + h), t + h) \cdot D\mathcal{F}^h(x_0)\mathcal{N}(x_0, \tau)| \geqslant e^{\lambda_u h} \tag{12}$$

where $(x(\tau + h), \tau + h)$ is the trajectory passing through (x_0, τ) in the extended state space. Figure 10 shows a sketch of an unstable material surface over the time interval I_u. N is called a stable material surface if it is an unstable material surface in the sense of equation (12) backwards in time. An unstable (respectively, stable) material line with instability interval I_u (respectively, stability interval I_s) is a curve Γ_t which generates an unstable (respectively, stable) material surface in the extended state space. Unstable and stable material lines and surfaces are referred to as *hyperbolic material lines* and *hyperbolic material surfaces*, respectively. Their associated intervals I_u and I_s are referred to as *hyperbolicity intervals*. Hyperbolic material surfaces are never unique on a finite-time interval. However, if they are unstable for a sufficiently long time interval, they will appear unique up to numerically unresolvable errors. Thus, stable and unstable material surfaces will be used in the definition of coherent structure boundaries. The results outlined above have also been extended to the 3D setting (Haller, 2001).

3.3.4. *Detecting coherent structure boundaries* For any initial condition x_0 at time $t_0 \in [t_{-1}, t_1]$, consider the maximal open set, $\mathcal{I}_u(x_0)$, within $[t_0, t_1]$ on which the instability condition equation (12) is satisfied. The instability time $T_u(x_0, t_0)$ associated with x_0 over the time interval $[t_0, t_1]$ is defined as

$$T_u(x_0, t_0) = \frac{1}{t_1 - t_0} \int_{\mathcal{I}_u(x_0)} dt$$

That is, T_u is the fraction of the time $t_1 - t_0$, for which the instability condition equation (12) holds. Similarly, the maximal open set, $\mathcal{I}_s(x_0)$, within $[t_0, t_{-1}]$, on which the instability condition equation (12) is satisfied in backward time, defines the stability time $T_s(x_0,t_0)$ associated with x_0 over the backward time interval $[t_0, t_{-1}]$ as

$$T_s(x_0, t_0) = \frac{1}{t_0 - t_{-1}} \int_{\mathcal{I}_s(x_0)} dt$$

$T_u(x_0, t_0)$ and $T_s(x_0, t_0)$ are called the *hyperbolicity times* associated with x_0 at t_0. With these definitions, coherent structure boundaries at $t = t_0$ are given by stable and unstable material lines along which T_s or T_u attains local extrema. In the next section, the fields T_s and T_u are plotted for studying mixing properties in controlled 2D channel flow. It is interesting to note, that for time periodic velocity fields, the coherent structure boundaries defined above coincide with the stable and unstable manifolds of hyperbolic fixed points of the corresponding Poincaré map.

4. Destabilization

4.1. *2D channel flow*

Mixing is commonly induced by means of open loop methods such as mechanical stirring, jet injection or mixing valves. These methods may use excessive amounts of energy, which in certain cases is undesirable. In Aamo *et al.* (2001), it is proposed to use active feedback control on the boundary of a 2D channel flow, in order to exploit the natural tendency in the flow to mix. In Aamo (2002) (Section 6.3.2) it was demonstrated that the very simple control law,

$$v_{\text{wall}} = k_v \Delta p \tag{13}$$

has a significant stabilizing influence on the 2D channel flow. In this section, we explore the behavior of the flow when k_v is chosen such that this feedback destabilizes the flow rather than stabilizes it. The conjecture is that the flow will develop a complicated pattern in which mixing will occur. 2D simulations are performed at $R = 6000$, for which the parabolic equilibrium profile is unstable. The vorticity map for the fully established flow (uncontrolled) at this Reynolds number is shown in the topmost graph in Figure 11. This is the initial data for the simulations. Some mixing might be expected in this flow, as it periodically ejects vorticity into the core of the channel. The objective, however, is to enhance the mixing process by boundary control, which we impose by setting $k_v = 0.1$ in equation (13). The vorticity maps in Figure 11 suggest that the flow pattern becomes considerably more complicated as a result of the control. The upper-left and upper-right graphs in Figure 12 show the perturbation energy, $E(\mathbf{w})$, and enstrophy as functions of time. The former increases by a factor of 5 , while the latter is doubled. It is interesting to notice that the control leading to such an agitated flow is small (see lower-left graph in Figure 12). The maximum value of the control flow kinetic energy is less than 0.7% of the perturbation kinetic energy of the uncontrolled flow, and only about 0.1% of the fully developed, mixed (controlled) flow! Next, we will quantify the mixing in a more rigorous way, by studying the movement of passive tracer particles, representing dye blobs.

The location of the dye as a function of time completely describes the mixing,

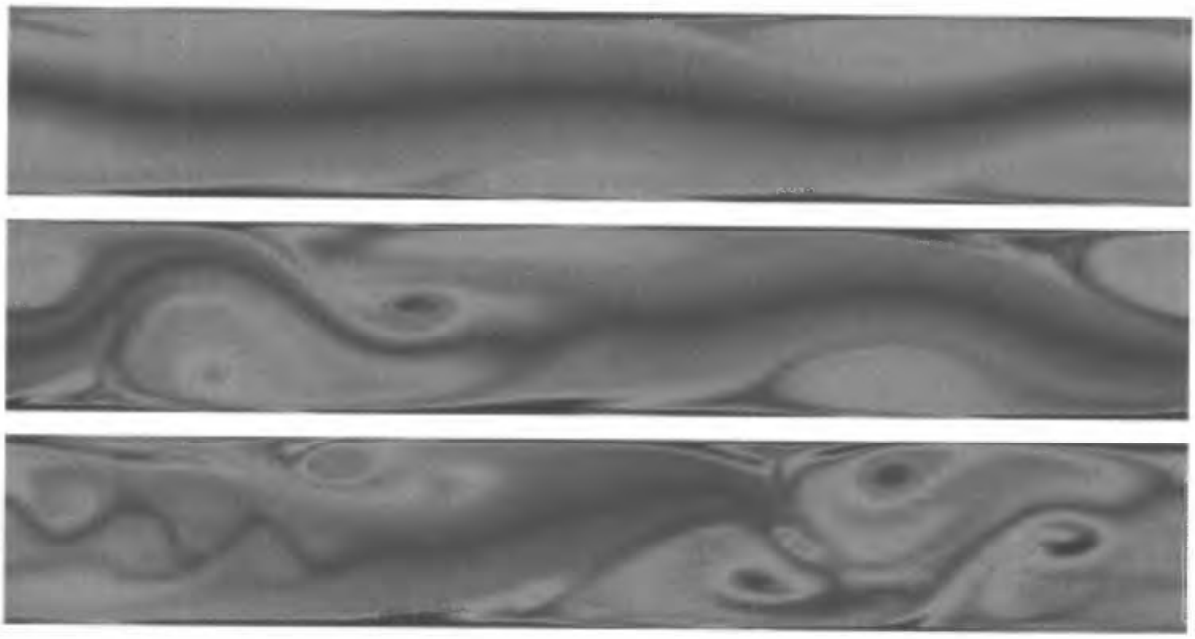

Figure 11. Vorticity map for the fully established, uncontrolled, channel flow ar $Re = 6000$ (top), and for the controlled case at $t = 50$ (middle) and $t = 80$ (bottom).

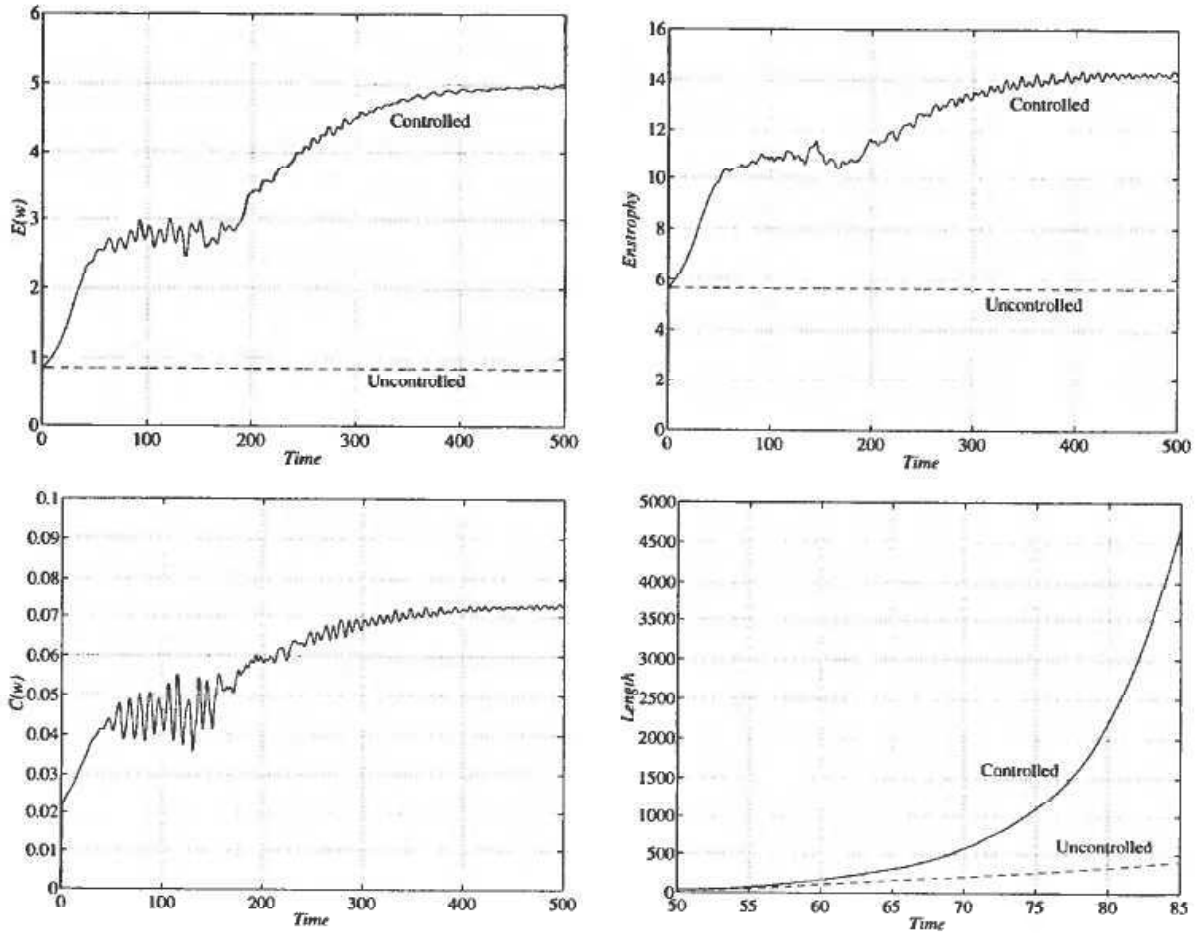

Figure 12. Energy $E(\mathbf{w})$ (top left), enstropy (top right), control effort $C(\mathbf{w})$ (bottom left), and dye surface length (bottom right), as functions of timc.

but in a flow that mixes well, the length of the interface between the dye and the fluid increases exponentially with time. Thus, calculating the location of the dye for large times is not feasible within the restrictions of modest computer resources (Franjione and Ottino, 1987). We do, nevertheless, attempt this for small times, and supplement the results with less accurate, but computationally feasible, calculations for larger times. A particle-line method, loosely based on Ten *et al.* (1998) and Krasnopolskaya *et al.* (1999), is used to track the dye interface. In short, this method represents the interface as a number of particles connected by straight lines. The positions of the particles are governed by the equation $dX/dt = (U(X,t), V(X,t))$, where X is a vector of particle positions. At the beginning of each time step, new particles are added such that at the end of the time step, a prescribed resolution, given in terms of the maximum length between neighboring particles, is maintained. The fact that we are working with a single fluid representing multiple miscible fluids, ensures that dye surfaces remain connected (Ottino, 1990). At $t = 50$, when the perturbation energy is about tripled in the controlled case (Figure 12), eighteen blobs are distributed along the centerline of the channel as shown in Figure 13. They cover 25% of the total domain. Figure 14 compares the configuration of the dye in the uncontrolled and controlled cases for 5 time instances. The difference in complexity is clear, however, large regions are poorly mixed even at $t = 85$. The lower-right graph

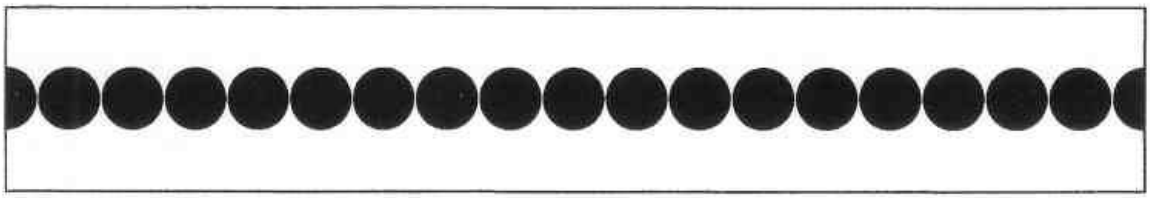

Figure 13. Initial distribution of dye blobs (at $t = 50$).

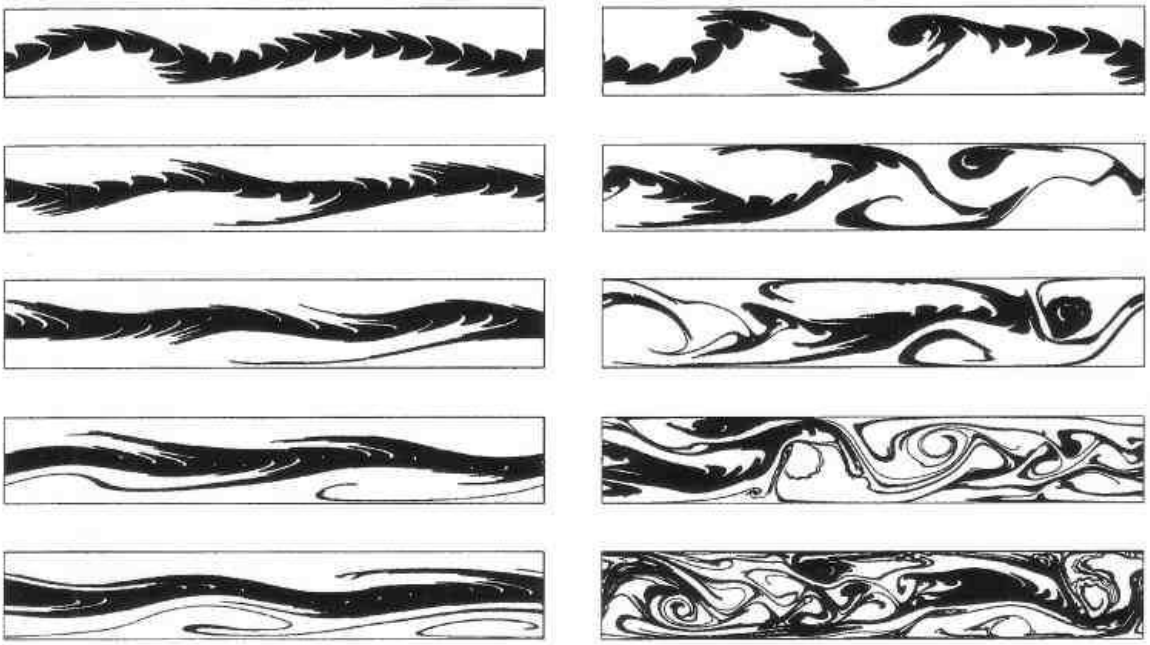

Figure 14. Dye distribution for uncontrolled flow (left column) versus controlled flow (right column) at $t = 55$, 60, 65, 75 and 85 (from top towards bottom).

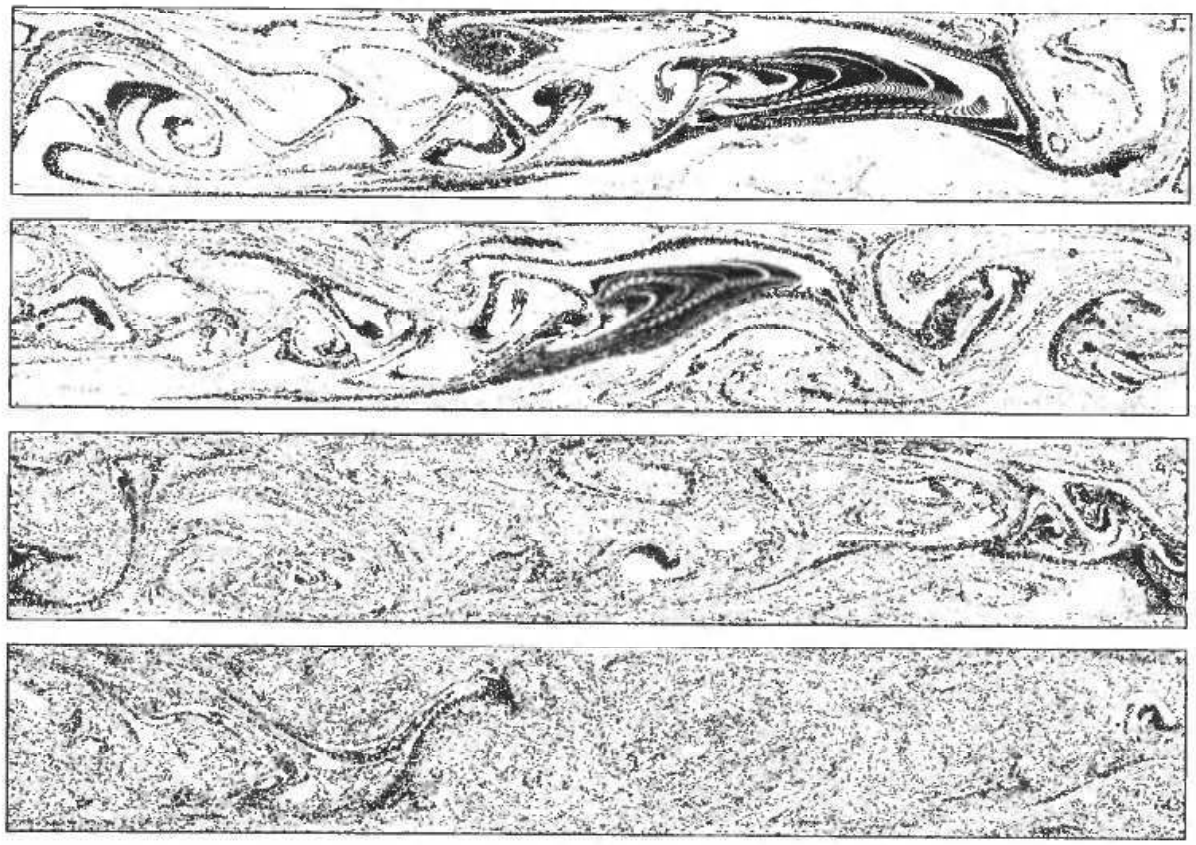

Figure 15. Particle distribution for controlled flow at $t = 85$, 100, 125 and 150 (from top towards bottom).

in Figure 12 shows the total length of the surface of the dye. The length appears to grow linearly with time in the uncontrolled case, whereas for the controlled case, it grows much faster, reaching values an order of magnitude larger than in the uncontrolled case. In order to approximate the dye distribution for large time, a fixed number of particles are uniformly distributed throughout the domain, distinguishing between particles placed on the inside (*black* particles) and on the outside (*white* particles) of regions occupied by dye. Figure 15 shows the distribution of black particles at $t = 85$ (for comparison with Figure 14), 100, 125 and 150. The particle distribution becomes increasingly uniform.

In order to quantify the mixing further, we ask the following question: given a box of size ε, what is the probability, P, of the fluid inside being *well mixed*? An appropriate choice of ε, and what is considered well mixed, are application specific parameters, and are usually given by requirements of some downstream process. In our case, the blobs initially cover 25% of the domain, so we will define *well mixed* to mean that the dye covers between 20% and 30% of the area of the box. The size ε of the boxes will be given in terms of pixels along one side of the box, so that the box covers ε^2 pixels out of a total of 2415×419 pixels for the entire domain. On this canvas, the box may be placed in $(419 - (\varepsilon - 1)) \times 2415$ different locations. The fraction of area covered by dye inside box i of size ε, is for small times calculated according to

$$c_\varepsilon^i = \frac{n_p}{\varepsilon^2} \tag{14}$$

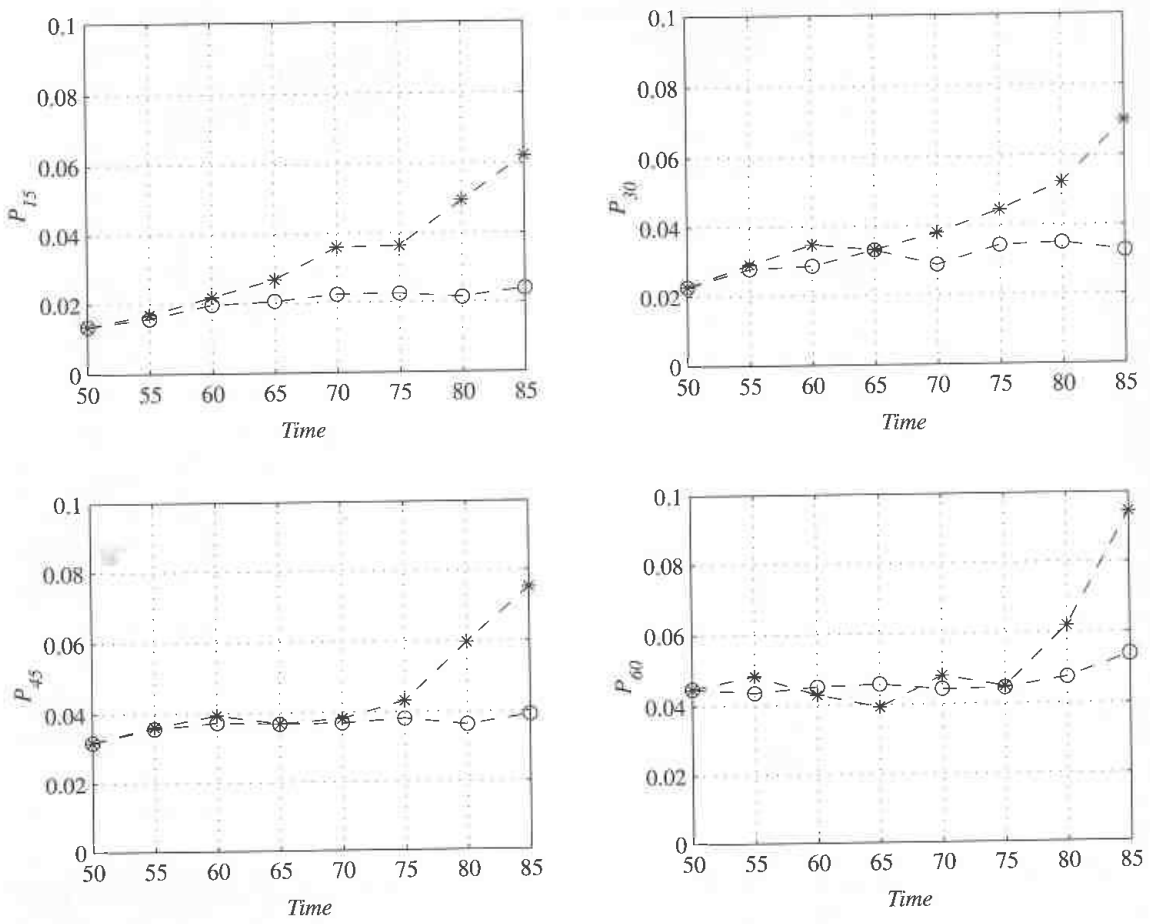

Figure 16. Probability of well mixedness for the uncontrolled case (○) and controlled case (∗).

where n_p is the number of pixels covered by dye, and for large times according to

$$c_\varepsilon^i = \frac{n_b}{n_w + n_b} \tag{15}$$

where n_b and n_w denote the number of black and white particles, respectively, contained in the box. P , which depends on ε, is calculated as follows

$$P_\varepsilon = \frac{1}{n} \sum_{i=1}^{n} \text{eval}(0.2 < c_\varepsilon^i < 0.3) \tag{16}$$

where n is the total number of boxes. The expression in the summation evaluates to 1 when $0.2 < c_\varepsilon^i < 0.3$ and 0 otherwise. For small times $n = (419 - (\varepsilon - 1)) \times 2415$, whereas for large times n may be smaller as we choose to ignore boxes containing less than 25 particles. Figures 16 and 17 show P_ε as a function of time for $\varepsilon \in [15, 30, 45, 60]$. In Figure 18, the hyperbolicity times of a grid of uniformly distributed initial conditions at $t_0 = 100$ are shown (see Section 3.3.4 for the definition of hyperbolicity time). The geometry of the coherent structure boundaries become considerable more complex in the controlled case, indicating extensive stretching and folding of material elements in the flow.

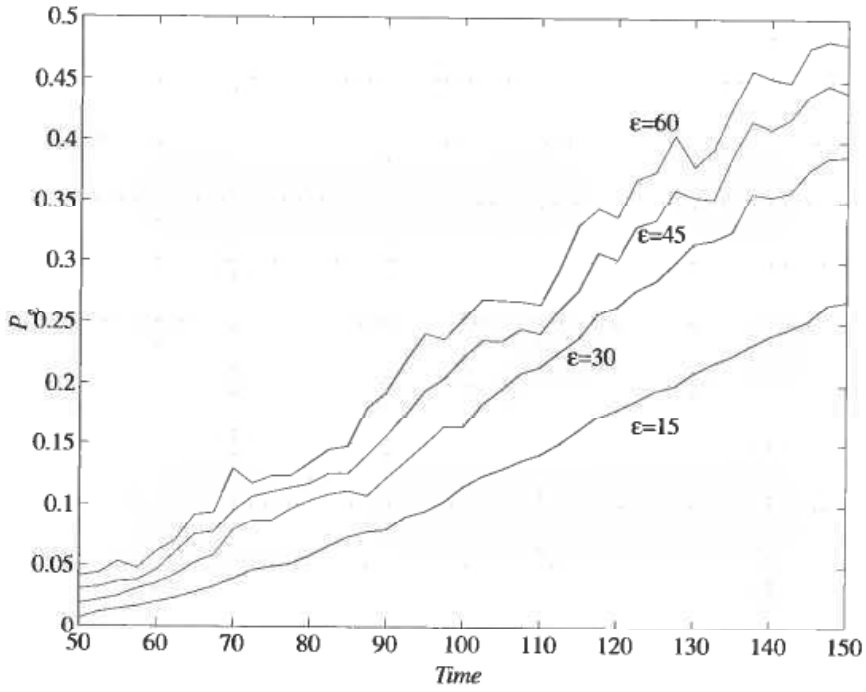

Figure 17. Probability of well mixedness for the controlled case based on uniform particle distribution.

4.2. *3D pipe flow*

Recently, the results of the previous section have been generalized to 3D pipe flow (Balogh *et al.*, 2001). The control law designed in Aamo (2002, Section 6.3.2), with an appropriately selected feedback gain, was used, that is

$$v_r(1,\theta,z,t) = k\,(p(1,\theta,z,t) - p(1,\theta+\pi,z,t)) \tag{17}$$

Simulations were performed at $Re = 2100$, which is slightly higher than the limiting number $Re = 2000$ for nonlinear stability. Figure 19 shows that the control results in an approximately 50 increase in the perturbation energy and 92 almost instantaneous increase in the enstrophy.

The instantaneous streamwise vorticity along a cross section of the pipe (Figure 20) also shows some promise for increased mixing with higher values of vorticity and more complex vortex structures in the controlled case than in the uncontrolled case. Vorticity is increased not only near the wall but everywhere in the pipe.

The method used to quantify and visualize mixing is the tracking of dye in the flow, as done for the 2D case in the previous section. A passive tracer dye is introduced along the center of the pipe represented by a set of 100 particles (Figure 21). The position of these particles is traced using a particle–line method (Krasnopolskaya *et al.*, 1999, Ten *et al.*, 1998). The distance between neighboring particles is kept under 0.1 by introducing new particles to halve the distance if necessary to obtain a connected dye surface at all time. As shown in Figure 22, the number of particles, that is, the length of the dye, increases in the controlled case at a much higher rate than in the uncontrolled case. Adding particles is not feasible computationally for an extended period of time. Addition of particles was stopped when their number reached two million ($t = 4$ in the controlled case and $t = 8$ in the uncontrolled case), but the tracking of them continued. Figure 23 shows the distribution of particles inside the pipe. In the controlled case a more uniform particle distribution was obtained even for smaller time.

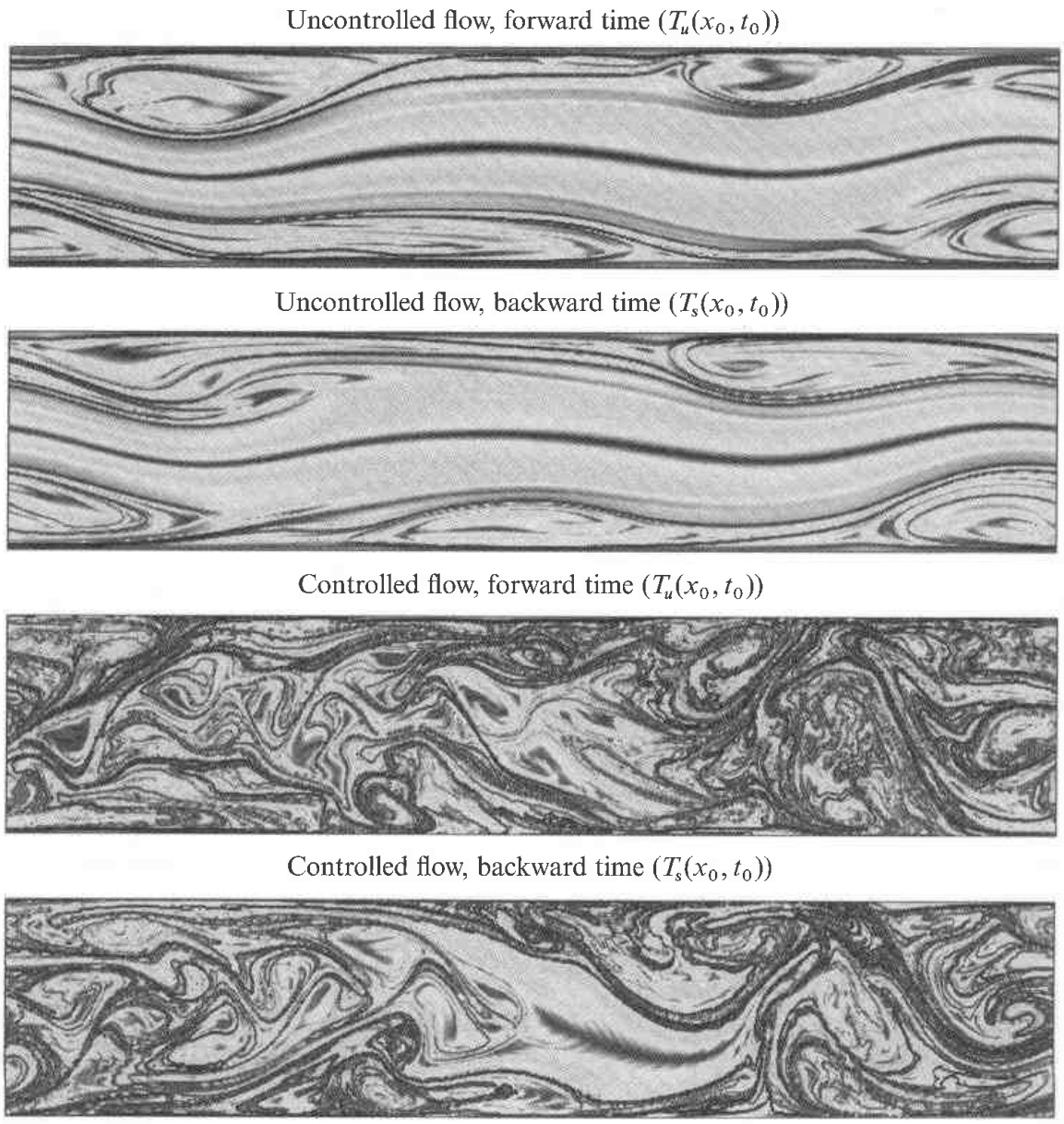

Figure 18. Hyperbolicity times for uncontrolled (upper two graphs) and controlled (lower two graphs) channel flow at $t_0 = 100$.

In Balogh *et al.* (2001), the control law equation (17) was also shown to exhibit certain optimality properties.

5. Concluding Remarks

The field of flow control has picked up pace over the past decade or so, on the promise of real-time distributed control on turbulent scales being realizable in the near future. This promise is due to the micromachining technology that emerged in the 1980s, and developed at an amazing speed through the 1990s. In lab experiments, so called micro-electro-mechanical systems (MEMS) that incorporate the entire detection-decision-actuation process on a single chip, have been batch processed in large numbers and assembled into flexible skins for gluing onto body-fluid interfaces for drag reduction purposes.

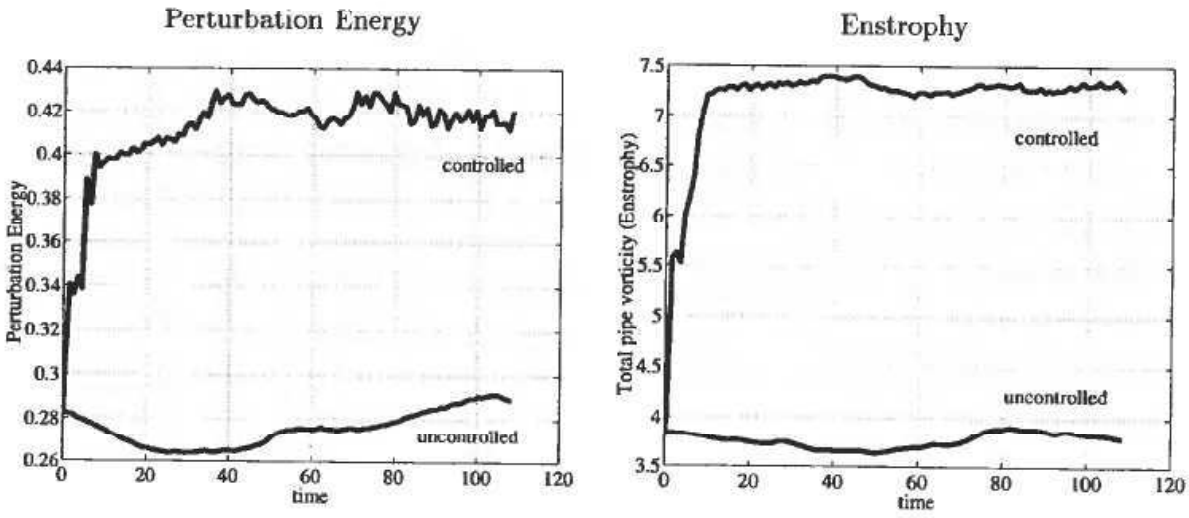

Figure 19. Perturbation energy and enstrophy.

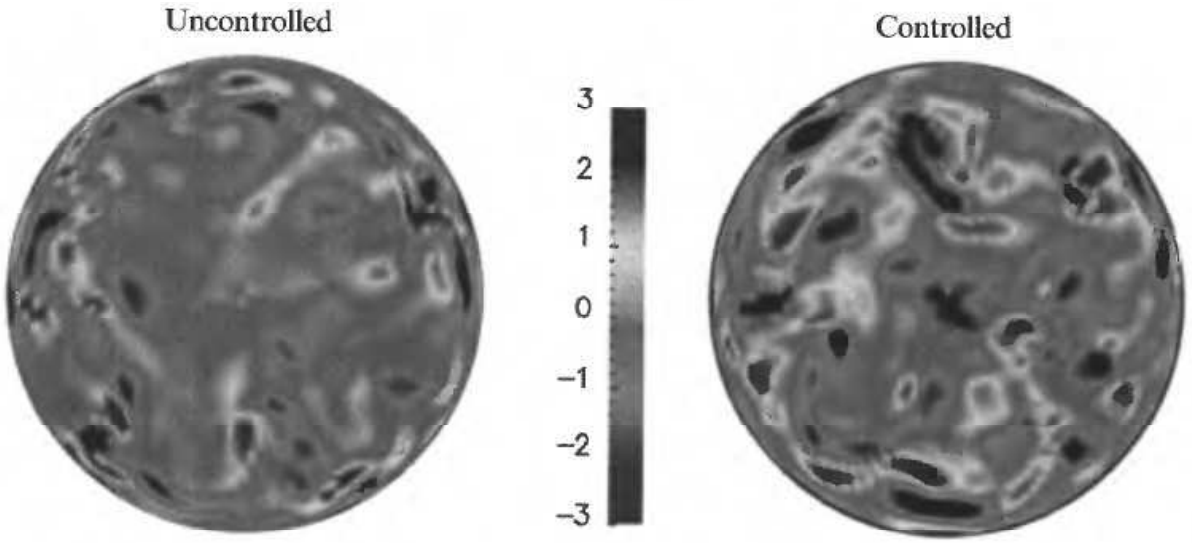

Figure 20. Streamwise vorticity.

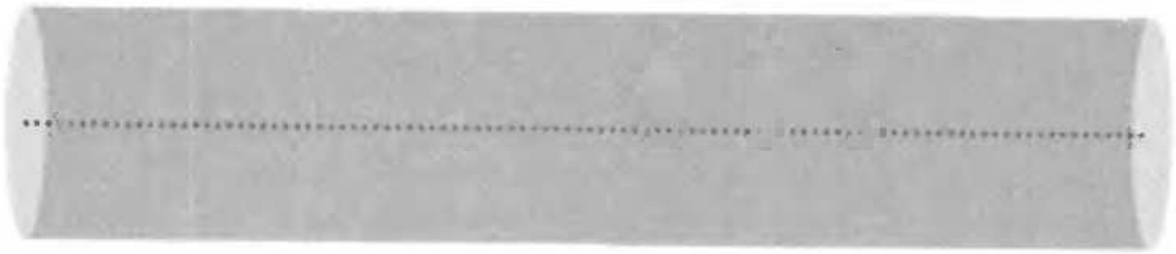

Figure 21. Initial particle distribution.

Control of fluid flows span a wide variety of specialities. In Part II of this tutorial, we have focused on diagnostics of mixing and the problem of enhancing mixing by boundary feedback control. Diagnostic tools from dynamical systems theory have been presented that enable detection and quantification of chaotic transport in periodically perturbed systems. However, real systems are generally not periodic, and

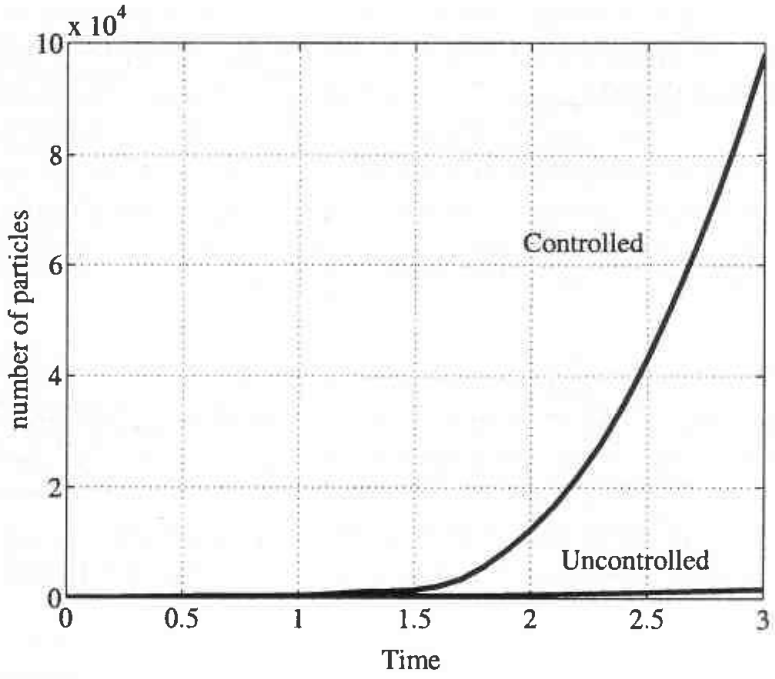

Figure 22. Length of dye as a function of time.

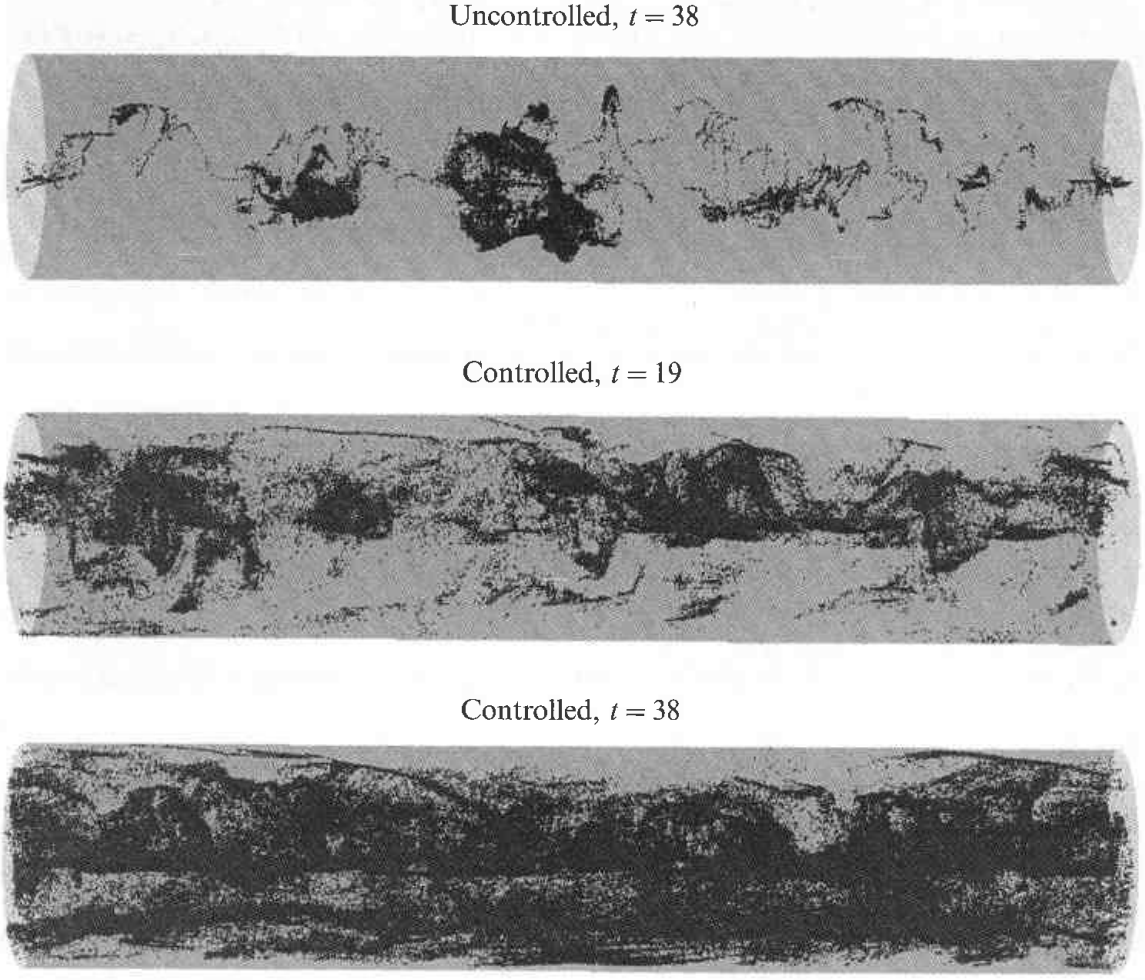

Figure 23. Particle distribution.

available measurements or simulations are finite in time. A method for quantifying mixing in finite-time velocity fields has been discussed, and applied to data obtained from simulations of the 2D controlled channel flow. Mixing has traditionally been brought on by open-loop control strategies, such as stirring, jet injection or mixing valves. Applications of active feedback to mixing problems are scarce in the literature, but the idea is currently drawing attention from various research groups. Feedback laws for the purpose of mixing enhancement in 2D and 3D pipe flow have been presented, and simulations show that they induce strong mixing.

Acknowledgements

The authors would like to thank Drs. Andras Balogh (UCSD), Yong Wang (Brown University), and Vered Rom-Kedar (Weizmann Institute, Israel) for permitting reproduction of selected figures from their work, and Dr. Svein Ivar Sagatun (Norsk Hydro) for valuable comments during the preparation of this tutorial. The support from Norsk Hydro and the Norwegian Research Council is gratefully acknowledged.

References

Aamo, O. M., Krstić, M. and Bewley, T. R. (2002). Control of Mixing by Boundary Feedback in 2D Channel Flow. Submitted.

Aamo, O. M. (2002). Tutorial on Feedback Control of Flows, Part I: Stabilization of Fluid Flows in Channels and Pipes. *Modelling, Identification and Control*, **23**(3).

Annaswamy, A. M. and Ghoniem, A. F. (1995). Active Control in Combustion Systems. *IEEE Control Systems*, **15**(6), 49–63.

Aref, H. (1984). Stirring by chaotic advection. *Journal of Fluid Mechanics*, **143**, 1–21.

Aref, H. and Tryggvason, G. (1984). Vortex dynamics of passive and active interfaces. *Physica*, **12D**, 59–70.

Balogh, A., Aamo, O. M. and Krstić, M. (2002). Optimal Mixing Enhancement in 3D Pipe Flow. Submitted.

Bamieh, B., Mezić, I. and Fardad, M. (2001). A framework for destabilization of dynamical systems and mixing enhancement. In *Proceedings of the 49th IEEE Conference on Decision and Control*, Orlando, Florida USA.

Chien, W.-L., Rising, H. and Ottino, J. M. (1986). Laminar mixing and chaotic mixing in several cavity flows. *Journal of Fluid Mechanics*, **170**, 355–377.

D'Alessandro, D., Dahleh, M. and Mezić, I. (1998). Control of Fluid Mixing Using Entropy Methods. In *Proceedings of the American Control Conference*, Philadelphia, Pennsylvania.

D'Alessandro, D., Dahleh, M. and Mezić, I. (1999) Control of Mixing in Fluid Flow: A Maximum Entropy Approach. *IEEE Transactions on Automatic Control*, **44**(10), 1852–1863.

Franjione, J. G. and Ottino, J. M. (1987?). Feasibility of numerical tracking of material lines and surfaces in chaotic flows. *Phys. Fluids*, **30**, 3641–3.

Ghoniem, A. F. and Ng, K. K. (1987). Numerical study of the dynamics of a forced shear layer. *Phys. Fluids*, **30**(3), 706–721.

Guckenheimer, J. and Holmes, P. (1983). *Nonlinear Oscillations, Dynamical Systems, and Bifurcations of Vector Fields*. Springer-Verlag.

Haller, G. and Poje, A. C. (1998). Finite time transport in aperiodic flows. *Physica D*, **119**, 352–380.

Haller, G. (2000). Finding finite-time invariant manifolds in two-dimensional velocity fields. *Chaos*, **10**(1).

Haller, G. and Yuan, G. (2000). Lagrangian coherent structures and mixing in two-dimensional turbulence. *Physica D*, **147**, 352–370.

Haller, G. (2001). Distinguished material surfaces and coherent structures in three-dimensional fluid flows. *Physica D*, **149**, 248–277.

KHAKHAR, D. V., RISING, H. and OTTINO, J. M. (1986). Analysis of chaotic mixing in two model systems. *Journal of Fluid Mechanics*, **172**, 419–451.

KRASNOPOLSKAYA, T. S., MELESHKO, V. V., PETERS, G. W. M AND MEIJER, H. E. H. (1999). Mixing in Stokes flow in an annular wedge cavity. *Eur. J. Mech. B/Fluids*, **18**, 793–822.

LEONG, C. W. and OTTINO, J. M. (1989). Experiments on mixing due to chaotic advection in a cavity. *Journal of Fluid Mechanics*, **209**, 463–499.

MALHOTRA, N., MEZIĆ, I. and WIGGINS, S. (1998). Patchiness: A new diagnostic for Lagrangian trajectory analysis in time-dependent fluid flows. *International Journal of Bifurcation and Chaos*, **8**(6), 1053–1093.

MEZIĆ, C. (1994). *On Geometrical and Statistical Properties of Dynamical Systems: Theory and Applications*. Ph.D. thesis, California Institute of Technology.

MEZIĆ, I. and WIGGINS, S. (1999). A method for visualization of invariant sets of dynamical systems based on the ergodic partition. *Chaos*, **9**(1), 213–218.

MILLER, P. D., JONES, C. K. R. T., ROGERSON, A. M. and PRATT. L. J. (1997). Quantifying transport in numerically generated velocity fields. *Physica D*, **110**, 105–122.

NOACK, B. R., MEZIĆ, I. and BANASZUK, A. (2000). Controlling vortex motion and chaotic advection. In *Proceedings of the 39th IEEE Conference on Decision and Control*, Sydney, Australia, 11–15 December, 2000.

OTTINO, J. M. (1989). *The Kinematics of Mixing: Stretching, Chaos, and Transport*. Cambridge University Press.

OTTINO, J. M. (1990). Mixing, chaotic advection, and turbulence. *Annu. Rev. Fluid Mech.* **22**, 207–53.

POJE, A. C., HALLER, G. and MEZIĆ, I. (1999). The geometry and statistics of mixing in aperiodic flows. *Physics of Fluids*, **11**(10).

POJE, A. C. and HALLER, G. (1999). Geometry of Cross-Stream Mixing in a Double-Gyre Ocean Model. *Journal of Physical Oceanography*, **29**, 1469–1665.

ROM-KEDAR, V., LEONARD, A. and WIGGINS, S. (1990). An analytical study of transport, mixing and chaos in an unsteady vortical flow. *Journal of Fluid Mechanics*, **214**, 347–394.

SWANSON, P. D. and OTTINO, J. M. (1990). A comparative computational and experimental study of chaotic mixing of viscous fluids. *Journal of Fluid Mechanics*, **213**, 227–249.

TEN, A. A., PODLADCHIKOV, Y. Y., YUEN, D. A., LARSEN, T. B. and MALEVSKY, A. V. (1998). Comparison of Mixing Properties in Convection with the Particle-Line Method. *Geophys. Res. Lett.*, **25**, 3205–3208.

WIGGINS, S. (1990). *Introduction to Applied Nonlinear Dynamical Systems and Chaos*. Springer-Verlag.

WIGGINS, S. (1992). *Chaotic Transport in Dynamical Systems*. Springer-Verlag.